Climatology of the Residual Mean Circulation of the Martian Atmosphere and Contributions of Resolved and Unresolved Waves Based on EMARS

Anzu Asumi[1], Kaoru Sato[1], Masashi Kohma[1], and Yoshi-Yuki Hayashi[2]

[1]Department of Earth and Planetary Science, Graduate School of Science, The University of Tokyo, Tokyo 1130033, Japan; [2]Department of Planetology/Center for Planetary Science, Graduate School of Science, Kobe University, Hyogo 6500047, Japan

Corresponding author: Anzu Asumi (asumi@eps.s.u-tokyo.ac.jp)

Key Points:

- Climatology of the residual mean circulation of the Martian atmosphere is revealed based on the EMARS reanalysis dataset.
- Along with the resolved wave contribution, the subgrid-scale wave contribution to the residual mean circulation is estimated indirectly.
- Results suggest that small-scale waves such as gravity waves have more impact on driving the residual mean circulation on Mars than on Earth.

Abstract

The objective of this study was to examine both the climatology of the residual mean circulation, and the roles of resolved wave (RW) and unresolved wave (UW) forcings over four Mars years, based on the transformed Eulerian mean equation system using the EMARS reanalysis dataset. While RW forcing was estimated directly as Eliassen–Palm flux divergence, the forcing by UWs, including subgrid-scale gravity waves, was estimated indirectly using the zonal momentum equation. This indirect method, devised originally for study of Earth's middle atmosphere, is applicable to latitudinal regions having angular momentum isopleths connected from the surface to the top of the atmosphere, which are usually mid- and high-latitude regions. In low latitudes of the winter hemisphere, a strong residual mean poleward flow is observed at an altitude range of 40–80 km, where the latitudinal gradient of the absolute angular momentum is small. The strong poleward flow crosses the isopleths of angular momentum in the regions of its northern and southern ends, indicating the necessity of the wave forcing. Our results suggest that the structure of the residual mean circulation at mid- and high-latitude regions is largely determined by UW forcing, particularly above the altitude of 60 km, whereas the RW contribution is also large below the altitude of 60 km.

Plain Language Summary

The Lagrangian mean general circulation is important in determining the distributions of mass and temperature in a planetary atmosphere. However, few studies have investigated the climatological seasonal mean features for Mars using reanalysis datasets. The purpose of this study was to use the EMARS reanalysis dataset to examine the general circulation of Mars and its driving mechanism based on the transformed Eulerian mean equation theory. We estimated the contribution of resolved waves (RWs) in the reanalysis dataset directly as Eliassen–Palm flux divergence, and that of unresolved waves (UWs) including subgrid-scale gravity waves using an indirect method devised originally for Earth atmosphere studies. The results suggest that the entire structure of the general circulation is largely determined by UW forcing, particularly at altitudes above 60 km, although the contribution of RWs is also large at altitudes below 60 km.

1 Introduction

The Lagrangian mean meridional circulation is important in determining both the distributions of mass and minor constituents and the thermal structure of a planetary atmosphere.

For Earth's atmosphere, the transformed Eulerian mean (TEM) equation system (e.g., Andrews et al., 1987) is often used to examine the residual mean flow, which is a reasonable approximation of the Lagrangian mean flow (Dunkerton, 1983). This equation system can also be applied to the Martian atmosphere because of the similarity in the basic dynamical properties of both planets in terms of their physically and optically thin atmosphere with almost the same rotation rate and obliquity (e.g., Read et al., 2015).

The residual mean circulation in Earth's middle atmosphere is driven by momentum deposition associated with the breaking and/or dissipation of atmospheric waves such as Rossby waves and gravity waves (GWs) originating from the lower atmosphere as well as the diabatic heating due to radiation processes and phase change of atmospheric constituents (e.g., Plumb, 2002). The role of wave forcing to the residual mean flow can be examined using the downward control principle derived by Haynes et al. (1991), which indicates that the Coriolis torque for the residual mean meridional flow in the mid- and high latitudes is balanced with the wave forcing, and that the resultant circulation is formed below the wave forcing in a steady state.

Analyses on the residual mean circulation using this principle have been conducted for the Martian atmosphere but limited to specific seasons or phenomena. For example, based on the Martian general circulation model (MGCM), the residual mean circulation of the Martian atmosphere was investigated for cases when strong temperature inversions and warming were observed in the winter polar regions (e.g., Kuroda et al., 2009). Hartogh et al. (2007) suggested that planetary waves and thermal tides are the main contributors to the wave forcing that drives the circulation. Furthermore, Kuroda et al. (2009) showed that the contributions of resolved small-scale GWs and eddies to the Eliassen–Palm (EP) flux divergence in the MGCM are almost equal to those of thermal tides and planetary waves, at least in high winter latitudes during global dust storms. They also suggested that the contribution of GWs would be larger in simulations with higher model resolution. Specific phenomena such as the winter polar warming during global dust storm events as mentioned above have been studied extensively, whereas few studies have investigated the climatological, or in other words normal features of the meridional circulation. It should be noted that obtaining observations of physical quantities other than temperature is generally difficult, and that quantitative analysis based on such observations using the TEM equations is not easy.

Observations are usually not only limited for specific quantities but also sparsely distributed, meaning that reanalysis data produced by applying data assimilation techniques to such observations are commonly used in studies of Earth's weather and climate. Reanalysis datasets for Mars have recently become available, thereby allowing more quantitative analysis of the climatology of the general circulation of the Martian atmosphere. The first reanalysis dataset made available for Mars is the Mars Analysis Correction Data Assimilation (MACDA; Montabone et al., 2014), which covers the period 1999–2004, corresponding to the period from the late northern summer of Mars Year (MY) 24 to the late northern spring of MY 27. Using MACDA, Mitchell et al. (2015) examined the climatological nature of the zonal mean state of the atmosphere, e.g., the zonal mean temperature, zonal wind, residual mean flow, and especially the Martian polar vortices, and compared them with those on Earth. The second publicly available reanalysis dataset is the Ensemble Mars Atmosphere Reanalysis System (EMARS; Greybush et al., 2019) that covers more than seven MYs, i.e., longer than the period covered by MACDA. The climatology of the circulation of Mars has not yet been examined using EMARS. Moreover, detailed TEM equation analyses of the relation between wave forcing and residual mean flow have not yet been conducted using a reanalysis dataset.

Another advantage of TEM analysis using a reanalysis dataset is that every resolved wave (RW) forcing can be estimated piecewise as a form of the EP flux divergence. Additionally, it is possible to use the indirect method proposed by Sato and Hirano (2019) to estimate the contribution of unresolved processes to the residual mean flow. The unresolved process contribution reflects the parameterized GW forcing, the assimilation increment owing to the GW forcing that is not properly expressed by the GW parameterization, and model deficiency (Sato & Hirano, 2019). The potential contribution of unresolved waves (UWs) is large, as discussed by Kuroda et al. (2009) based on their MGCM study. Other modeling studies (e.g., Barnes, 1990, Joshi et al., 1995, Collins et al., 1997, Forget et al., 1999, Angelats I Coll et al., 2005) have shown the importance of GWs in determining the structure of the Martian atmosphere. However, the validity of the results of those model-based studies needs to be verified by observations.

Observational studies showed that more than 10% of the amplitude of the oscillation in both temperature and density is due to components with vertical and horizontal wavelengths shorter than 10 and 200 km above the altitude of 60 km in the Martian mesosphere, respectively, suggesting the dominance of GWs (Fritts et al., 2006; Magalhães et al., 1999). Applying the

method by Sato and Hirano (2019) to examine the contribution of unresolved processes to reanalysis datasets will provide important information on the possible roles of such GWs in relation to the residual circulation of the Martian atmosphere.

The present study examined the residual mean circulation of the Martian atmosphere for the annual mean and the seasonal mean climatology by following common methods based on the TEM equations used in studies of Earth's middle atmosphere. We used EMARS (Greybush et al., 2019) to examine both the climatological features of the zonal mean dynamical and thermal structures, and the contributions of resolved and unresolved processes quantitively.

The present paper is organized as follows. Brief descriptions of the data and the method of analysis used in the study are provided in section 2. The fundamental characteristics of the zonal mean fields are described in section 3. The contributions of RWs and unresolved processes in the residual mean meridional circulation are examined in sections 4 and 5, respectively and results are discussed. A summary and our concluding remarks are presented in section 6.

2. Method and Data description

2.1 EMARS

This study used temperature, zonal wind, meridional wind, and vertical velocity data extracted from the EMARS reanalysis dataset (Greybush et al., 2019). EMARS employs the Local Ensemble Transform Kalman Filter and assimilates atmospheric observations obtained using two instruments onboard Mars-orbiting spacecraft: the Thermal Emission Spectrometer (Smith, 2004) for MY 24–27, and the Mars Climate Sounder (McCleese et al., 2007) for MY 28–33. The Geophysical Fluid Dynamics Laboratory Mars Global Climate Model (e.g., Wilson & Hamilton, 1996; Greybush et al., 2012; Hoffman et al., 2010) is used as the numerical weather prediction model for the assimilation system. This model includes parameterization for orographic GWs (Waugh et al., 2016). The horizontal grid spacing is 6° longitudinally and 5° latitudinally. A hybrid sigma-pressure coordinate with the transition pressure level at 2 Pa is employed in the vertical. The number of pressure levels of the model is 28. The time interval of the reanalysis data is a Martian hour, which is one twenty fourth of a Mars sol. In this study, for ease of analysis, linear interpolation in the vertical was performed to convert the data to log-pressure coordinates taking a scale height of 10 km.

We analyzed EMARS data for MY 29–32. Data for the remaining MYs were not considered for the following three reasons. First, data for MY 24, 27, 28, and 33 contain many missing values. Second, MY 25 is exceptional because a global dust storm occurred. Third, the feature in the meridional cross sections of the zonal mean fields of MY 26 is different from that of the climatology based on MY 29–32, which might be attributable to differences between the data retrieval algorithm of the Thermal Emission Spectrometer (MY 24–27) and the Mars Climate Sounder (MY 28–33) (Greybush et al., 2019).

Figure 1 shows meridional cross sections of the zonal mean temperature ($\bar{T}$) and the zonal mean wind ($\bar{u}$) in the Northern Hemisphere (NH) winter for each of MY 29–32, where the overbar denotes the zonal mean. It is evident that the structure of the temperature profile, including the locations and values of the maxima and minima, is very similar between the four years. The similarity in structure is also evident for the zonal mean zonal wind in terms of the location and strength of both the easterly jet in the Southern Hemisphere (SH) and the westerly jet in the NH, although slight differences are noted in the jet peak values. Thus, in our study, the data for MY 29–32 were used to elucidate the climatological features for the annual mean and the seasonal mean of typical years without a global dust storm. The thermal inertia of the Martian climate is small. Therefore, seasonal variations within a certain year are less sensitive to the climatic conditions in previous years, unlike the situation on Earth owing to the presence of oceans. Thus, obtaining an average over just four years can capture the principal climatological characteristics of the Martian atmosphere. EMARS contains two types of gridded data: an "analysis" dataset and a "background" dataset. We used the background dataset with hourly outputs from MGCM forecasts in the data assimilation. Different from the analysis dataset, the background dataset provides all the physical quantities including vertical winds that are needed for the TEM analysis.

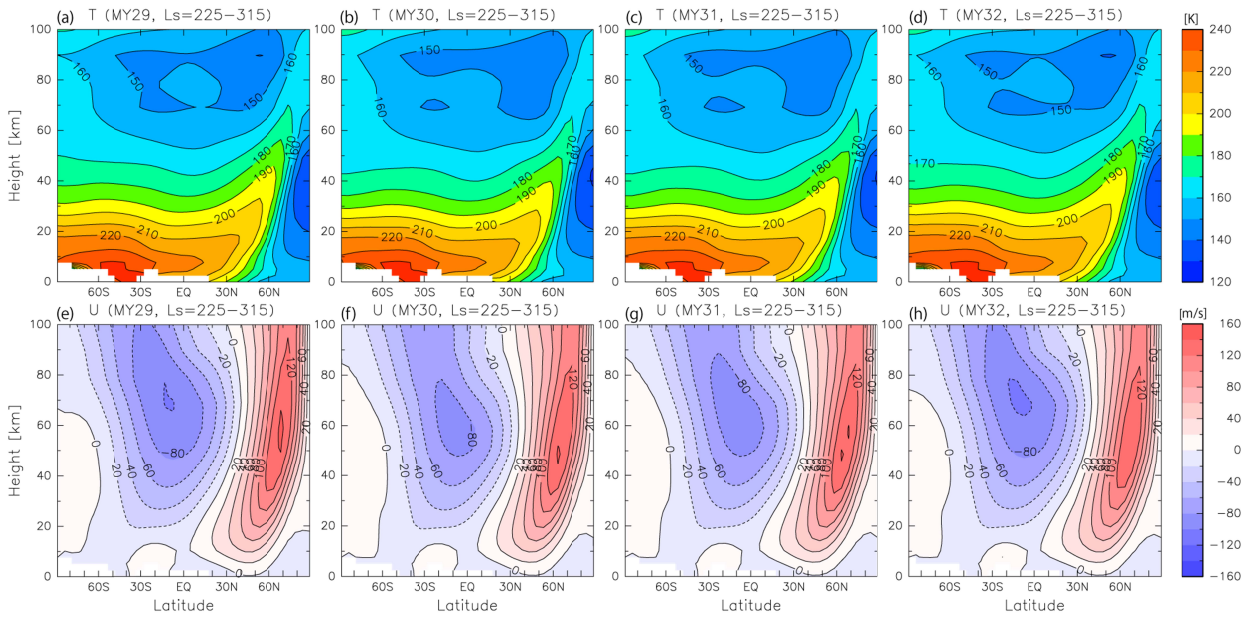

Figure 1. Latitude–height sections of zonal mean zonal temperature for NH winter in: (**a**) MY 29, (**b**) MY 30, (**c**) MY 31, and (**d**) MY 32. (**e**)–(**h**) Same as (**a**)–(**d**), respectively, but for zonal mean zonal wind.

In this study, a season was defined as follows. An MY was divided into four taking an areocentric longitude of 90° for the analysis. The solar longitudes of L_s = 0°, 90°, 180°, and 270° were defined as the NH spring equinox, summer solstice, autumn equinox, and winter solstice, respectively. Each season was defined as the period that spans between ±45° from L_s = 0°, 90°, 180°, or 270°, i.e., L_s = 315°–45° (NH spring), L_s = 45°–135° (NH summer), L_s = 135°–225° (NH autumn), and L_s = 225°–315° (NH winter). In this paper, the climatological features of the annual mean, NH summer, and NH winter are mainly shown and discussed.

2.2 Transformed Eulerian mean (TEM) equation system

The TEM equation system for spherical coordinates was used for the analysis (Andrews et al., 1987). The log-pressure coordinate is expressed as follows:

$$z = -H \log \frac{p}{p_s}, \qquad (1)$$

where p_s is surface pressure (p_s = 1000 Pa), H is the scale height ($H = \frac{RT_0}{g}$ = 10 km), T_0 is the typical atmospheric temperature (T_0 = 142 K), and R is the gas constant for the dry Martian air

($R = 191$ J/kg K). The zonal mean zonal momentum equation in the log-pressure coordinate is expressed as follows:

$$\frac{\partial \bar{u}}{\partial t} - \hat{f}\bar{v}^* + \bar{w}^* \frac{\partial \bar{u}}{\partial z} = \frac{1}{\rho_0 a \cos\phi} \nabla \cdot \boldsymbol{F} + \overline{\mathrm{X}}, \quad (2)$$

$$\hat{f} = f - \frac{1}{a\cos\phi} \frac{\partial (\bar{u}\cos\phi)}{\partial \phi}, \quad (3)$$

where $\bar{v}^*$ and $\bar{w}^*$ are the residual mean meridional and vertical flows, respectively, which are defined as follows:

$$\bar{v}^* \equiv \bar{v} - \frac{1}{\rho_0}\frac{\partial}{\partial z}\left(\rho_0 \frac{\overline{v'\theta'}}{\frac{\partial \theta_0}{\partial z}}\right) \text{ and } \bar{w}^* \equiv \bar{w} + \frac{1}{a\cos\phi}\frac{\partial}{\partial \phi}\left(\cos\phi \frac{\overline{v'\theta'}}{\frac{\partial \theta_0}{\partial z}}\right), \quad (4)$$

where ρ_0 is the basic density,

$$\rho_0(z) = \frac{p_s}{RT_s} e^{-\frac{z}{H}}, \quad (5)$$

a is the radius of Mars, f is the Coriolis parameter ($f = 2\Omega \sin\phi$), Ω is the rotation rate of Mars, and t and ϕ are time and latitude, respectively. EP flux $\boldsymbol{F}$ is defined as follows:

$$\boldsymbol{F} \equiv \left(0, \boldsymbol{F}^{(\phi)}, \boldsymbol{F}^{(z)}\right), \quad (6)$$

$$F^{(\phi)} \equiv \rho_0 a \cos\phi \left(\frac{\partial \bar{u}}{\partial z}\frac{\overline{v'\theta'}}{\frac{\partial \theta_0}{\partial z}} - \overline{v'u'}\right), \quad (7)$$

$$F^{(z)} \equiv \rho_0 a \cos\phi \left(f - \frac{\partial(\bar{u}\cos\phi)}{\partial\phi}\frac{\overline{v'\theta'}}{\frac{\partial \theta_0}{\partial z}} - \overline{w'u'}\right). \quad (8)$$

EP flux divergence is written as $\nabla \cdot \boldsymbol{F}$:

$$\nabla \cdot \boldsymbol{F} \equiv \frac{1}{a\cos\phi}\frac{\partial\left(\boldsymbol{F}^{(\phi)}\cos\phi\right)}{\partial\phi} + \frac{\partial \boldsymbol{F}^{(z)}}{\partial z} \quad (9)$$

and $\overline{\mathrm{X}}$ is friction and/or viscosity. Note that the residual mean flow ($\bar{v}^*, \bar{w}^*$) is a reasonable approximation of the Lagrangian mean flow (Dunkerton, 1983). The residual mean flow is the sum of the Eulerian mean flow $\bar{v}$ and the Stokes correction. The Stokes correction tends to be large for Rossby waves and small for both GWs and tides (e.g., Sato et al., 2013).

From the mean continuity equation:

$$\frac{1}{a\cos\phi}\frac{\partial(\bar{v}^*\cos\phi)}{\partial\phi}+\frac{1}{\rho_0}\frac{\partial(\rho_0\bar{w}^*)}{\partial z}=0, \quad (10)$$

193 a mass stream function of the residual mean flow $\bar{\Psi}^*$ is defined as follows:

$$\bar{v}^* \equiv -\frac{1}{\rho_0\cos\phi}\frac{\partial\bar{\Psi}^*}{\partial z} \text{ and } \bar{w}^* \equiv \frac{1}{\rho_0 a\cos\phi}\frac{\partial\bar{\Psi}^*}{\partial\phi}. \quad (11)$$

194 Approximately 25% of the Martian atmosphere decreases and increases due to condensation and
195 sublimation of the CO_2 atmosphere (Lewis et al., 1999, Haberle et al., 2017). Such notable mass
196 change occurs in fall and spring. In the analysis of the present study, we assumed that the
197 continuity equation is always satisfied because our focus was on the climatology of the annual
198 mean and in the NH summer and winter.

199 In the following analyses, we mainly examine the climatology for $\bar{T}$, $\bar{u}$, $\bar{v}$, $\bar{v}^*$, and $\bar{\Psi}^*$.
200 The zonal mean absolute angular momentum ($\bar{m}$) per unit mass (Haynes et al., 1991; Randel et
201 al., 2002) is also shown as an essential quantity to discuss the role of wave forcing:

$$\bar{m} = a\cos\phi\,(\bar{u} + a\cos\phi\,\Omega). \quad (12)$$

202 **2.3 Method of estimating unresolved waves (UWs)**

203 Theoretically, the first term $\frac{1}{\rho_0 a\cos\phi}\nabla\cdot\boldsymbol{F}$ on the right-hand side of Eq. (2) is the
204 divergence of EP flux associated with all waves including tides, Rossby waves, and GWs.
205 However, EMARS does not resolve all waves because of the coarse grid. Thus, only the part of
206 $\frac{1}{\rho_0 a\cos\phi}\nabla\cdot\boldsymbol{F}$ attributable to RWs such as tides and Rossby waves, whose EP flux is designated
207 as $\boldsymbol{F}_{(\mathrm{RW})}$, can be calculated. The part of EP flux associated with UWs such as GWs is designated
208 as $\boldsymbol{F}_{(\mathrm{UW})}$. Thus, $\nabla\cdot\boldsymbol{F}$ can be written as follows:

209 $$\nabla\cdot\boldsymbol{F} = \nabla\cdot\boldsymbol{F}_{(\mathrm{RW})} + \nabla\cdot\boldsymbol{F}_{(\mathrm{UW})}. \quad (13)$$

210 EP flux divergence due to UWs ($\nabla\cdot\boldsymbol{F}_{(\mathrm{UW})}$) cannot be calculated directly but can be
211 estimated indirectly using Eq. (2) as follows:

212 $$\frac{1}{\rho_0 a\cos\phi}\nabla\cdot\boldsymbol{F}_{(\mathrm{UW})} = \bar{u}_t - \hat{f}\bar{v}^* + \bar{w}^*\bar{u}_z - \frac{1}{\rho_0 a\cos\phi}\nabla\cdot\boldsymbol{F}_{(\mathrm{RW})}, \quad (14)$$

213 and ignoring eddy viscosity $\bar{X}$ (Sato & Hirano, 2019). The contribution of UWs to $\bar{\Psi}^*$ can also be
214 estimated indirectly as follows:

$$\overline{\Psi}^*(\phi,z) = -\cos\phi \int_z^\infty \rho_0 \overline{v}^* dz, \quad (15)$$

$$\overline{\Psi}^*_{\nabla\cdot\boldsymbol{F}_{(\mathrm{RW})}}(\phi,z) = -\int_z^\infty \left[\frac{\nabla\cdot\boldsymbol{F}_{(\mathrm{RW})}}{a\hat{f}}\right]_{\overline{m}} d\zeta, \quad (16)$$

and

$$\overline{\Psi}^*_{\overline{u}_t}(\phi,z) = \cos\phi \int_z^\infty \left[\frac{\rho_0}{\hat{f}}\frac{\partial\overline{u}}{\partial t}\right]_{\overline{m}} d\zeta, \quad (17)$$

as

$$\overline{\Psi}^*_{\nabla\cdot\boldsymbol{F}_{(\mathrm{UW})}}(\phi,z) = \overline{\Psi}^*(\phi,z) - \overline{\Psi}^*_{\nabla\cdot\boldsymbol{F}_{(\mathrm{RW})}}(\phi,z) - \overline{\Psi}^*_{\overline{u}_t}(\phi,z), \quad (18)$$

where $\int_z [\,]_{\overline{m}} d\zeta$ means vertical integration along a constant $\overline{m}$. With this vertical integration along a constant $\overline{m}$, instead of that along a constant ϕ, the vertical advection of zonal wind $\overline{w}^*\overline{u}_z$ in Eq. (2) is properly included in the estimation. The stream function $\overline{\Psi}^*(\phi,z)$ is calculated directly by integrating $\overline{v}^*$ in the vertical from the top where $\overline{\Psi}^*(\phi,\infty) = 0$. The contribution of RWs to $\overline{\Psi}^*(\phi,z)$ ($\overline{\Psi}^*_{\nabla\cdot\mathbf{F}(\mathrm{RW})}(\phi,z)$) and the contribution of the $\overline{u}$ tendency $\overline{\Psi}^*_{\overline{u}_t}(\phi,z)$ are also calculated directly from $\nabla\cdot\boldsymbol{F}_{(\mathrm{RW})}$ and $\frac{\partial\overline{u}}{\partial t}$, respectively, using the reanalysis data.

Note that this indirect method is applicable only for latitudes where vertical integration along a constant $\overline{m}$ is possible. This is usually limited to mid- and high-latitude regions where the angular momentum isopleths are connected from the surface to the top of the atmosphere, and where $\hat{f}$ is not too small. Thus, the results obtained in the present study are mainly for the off-equatorial region. Also note that the term $\nabla\cdot\boldsymbol{F}_{(\mathrm{UW})}$, estimated using Eq. (18) with reanalysis data, is the sum of the parameterized GW forcing and the assimilation increment, which is composed of the GW forcing that is not properly expressed by the GW parameterization or because of some model deficiency.

2.4 Method of extracting tidal waves from resolved waves (RWs)

The RWs are divided into tidal waves and other waves, and the contribution of each wave to the RW forcing ($\nabla\cdot\boldsymbol{F}_{(\mathrm{RW})}$) is examined. Tidal waves are extracted using the method of Yasui et al. (2016), which is also used for Earth's atmosphere. First, daily time series are constructed separately for each local time. Next, the long-period components are obtained from each daily time series using a lowpass filter with a cutoff period of 30 sols (Ls = ~15°). The lowpass-filtered daily time series for the respective local times are combined into a single time series at the original time interval. The time series defined in this way is designated the tidal component.

3. Overview of the Zonal Mean Fields of the Martian Atmosphere Obtained from EMARS

Before examining the residual mean circulation, the climatology of the basic zonal mean fields using EMARS is presented. Note that previous studies (e.g., Greybush et al., 2019) discussed the zonal mean temperature, meridional wind, and vertical wind fields for only a specific period.

3.1 Characteristics of the climatology of the zonal mean zonal wind

Figure 2 shows the climatology of zonal mean temperature ($\bar{T}$) and zonal wind ($\bar{u}$) in meridional cross sections for the annual mean, NH summer, and NH winter. The zonal wind $\bar{u}$ is approximately in thermal wind balance with $\bar{T}$ in the mid- and high latitudes. For the annual mean climatology, two westerly jets are observed in both the Northern and Southern hemispheres. The peak values of the two jets are ~72 m s^{-1} at 60°S (z = ~50 km) and ~80 m s^{-1} at 60°N (z = ~50 km). Additionally, an easterly jet is present in the tropical region, the latitudinal width of which depends on altitude, i.e., it is ~60° at z = ~40 km and 90° at z = ~90 km. The peak value of the easterly wind is 56 m s^{-1} at z = ~60 km near the equator.

In the NH winter, a quite strong westerly jet is observed in the mid- and high latitudes of the NH. Additionally, an easterly jet is present over the NH low latitudes to the SH mid-latitudes. The $\bar{u}$ structure in the NH summer is almost symmetric about the equator with that in the NH winter. However, the jet strengths are different: the westerly and easterly jets are stronger in the NH winter than in the NH summer. In the NH winter, the westerly jet peak value is ~140 m s^{-1} at ~70°N (z = ~60 km) and the easterly jet peak value is 94 m s^{-1} at ~10°S (z = ~65 km); in the NH summer, the westerly jet peak value is ~110 m s^{-1} at ~70°S (z = ~45 km) and the easterly jet peak value is 74 m s^{-1} at ~5°N (z = ~60 km).

Such a difference between the two solstitial seasons is likely related to the large eccentricity of the Mars orbit. The distance between Mars and the Sun is shorter in the NH winter than in the NH summer, causing a large latitudinal gradient in temperature that should be in thermal balance with the large vertical gradient of the zonal wind. These characteristics observed in $\bar{u}$ are consistent with those determined in previous studies using models (e.g., Barnes et al., 1996; Lewis & Read, 2003) and those obtained using the MACDA reanalysis dataset (Mitchell et al., 2015). However, there are slight differences in the location and the peak value of the zonal wind jets depending on the model and reanalysis dataset.

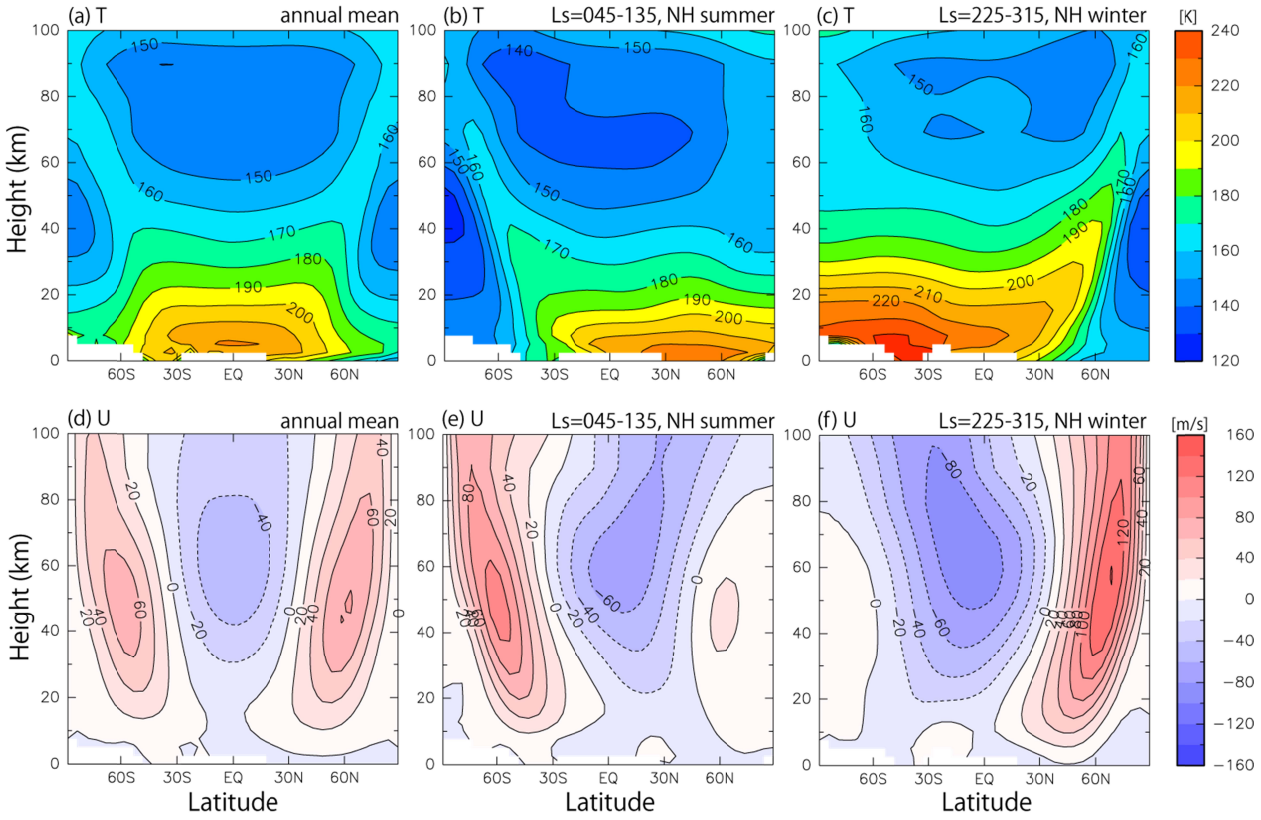

Figure 2. Latitude–height sections of zonal mean zonal temperature: (**a**) the annual mean, (**b**) in NH summer, and (**c**) in NH winter. (**d**)–(**f**) Same as (**a**)–(**c**), respectively, but for zonal mean zonal wind.

3.2 Comparison of the zonal mean meridional flow and the residual mean meridional flow

Figure 3 shows the climatology of $\bar{v}$ and $\bar{v}^*$ for the annual mean, NH summer, and NH winter. First, characteristics of $\bar{v}$ are described. For the annual mean climatology, $\bar{v}$ is poleward in both the NH and the SH, and almost symmetric about the equator above $z =$ ~30 km. The poleward flow is maximized at $z =$ ~55 km. The peak value of the northward flow in the NH (~9.9 m s^{-1} at 30°N) is slightly faster than that of the southward flow in the SH (~6.6 m s^{-1} at 30°S). The maximum latitude of the poleward flows is located at higher latitudes for higher altitudes. For altitudes of $z >$ ~80 km, the poleward flow maxima are located at ~70N and ~70S. The northward flow in the NH is weaker than the southward flow in the SH.

This hemispheric difference observed in the annual mean is attributable to the difference in the characteristics of $\bar{v}$ between the two solstitial seasons. In the NH summer, a southward

286 flow with a distinct peak of 19.2 m s^{-1} at 20°S (z = ~50 km) is dominant, whereas a northward
287 flow in the NH winter is more dominant and faster (28.5 m s^{-1} at its peak 20°N, z = ~55 km)
288 than the southward flow in the NH summer. It should be also noted that a strong counter flow is
289 observed below $z = 10$ km over a wide latitudinal range of approximately 60° around the
290 equator in both solstitial seasons.

291 The meridional flow from the summer hemisphere to the winter hemisphere at
292 approximately $z = 50$ km is similar to the deep branch of the Brewer–Dobson circulation in
293 Earth's stratosphere, although the latitudinal extension is wider on Mars. This result is consistent
294 with that shown by Mitchell et al. (2015), indicating that the stratosphere and mesosphere of
295 Earth are reasonably analogous to the Martian atmosphere. An interesting and notable feature is
296 that the meridional flow is much stronger in the Martian atmosphere than it is on Earth.

297 The characteristics observed in the structure of $\bar{v}$ and $\bar{v}^*$ are reasonably similar in the
298 altitude range of 10–90 km and the difference in magnitude is on the order of only a few meters
299 per second or less (Figure 3). This similarity between $\bar{v}$ and $\bar{v}^*$ is consistent with the findings of
300 previous studies (e.g., Barnes et al., 2017), and is strikingly different to the situation in Earth's
301 stratosphere. Such a small Stokes correction corresponding to the difference between $\bar{v}$ and $\bar{v}^*$
302 suggests that wave forcing caused by upward propagating Rossby waves is small.

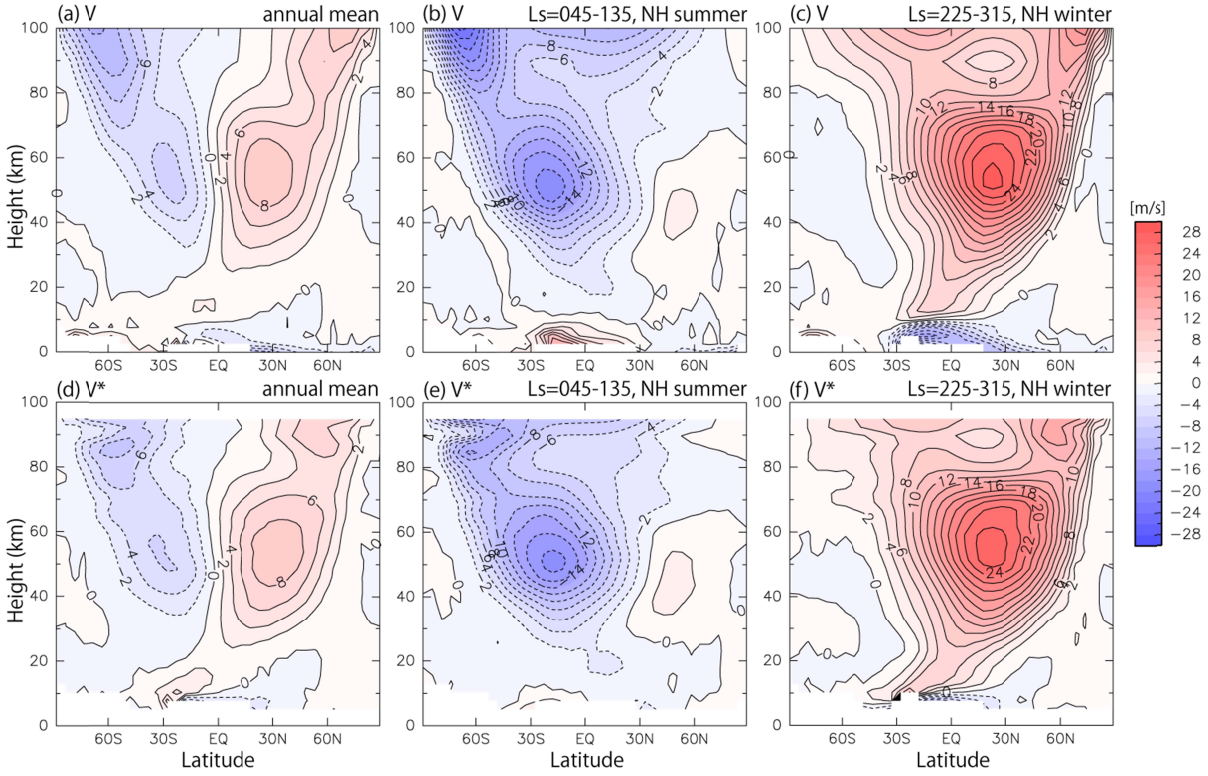

Figure 3. Latitude–height sections of zonal mean zonal meridional wind $\bar{v}$: (**a**) the annual mean, (**b**) in NH summer, and (**c**) in NH winter. (**d**)–(**f**) Same as (**a**)–(**c**)**,** respectively, but for residual mean meridional wind $\bar{v}^*$.

3.3 Structure of the residual mean mass stream function and its relation with the absolute angular momentum distribution

Figure 4 shows the meridional cross section of the climatology of $\bar{\Psi}^*$ and absolute angular momentum $\bar{m}$ for the annual mean, NH summer and NH winter. The Martian residual mean circulation varies drastically in the annual cycle (Lewis & Read, 2003; Read, 2011). As reported in many previous studies using the MGCM, and as expected from Figure 3d, the annual mean climatology of $\bar{\Psi}^*$ has roughly equatorially symmetric cells in the meridional cross section: clockwise in the NH and counterclockwise in the SH (Figure 4a). Closer inspection reveals that the NH circulation is stronger than the SH one, as is also observed in terms of $\bar{v}^*$ (Figure 3). Additionally, it is noteworthy that the upward branch is located slightly toward the SH side.

In the solstitial seasons, the winter circulation is large and strong: In the NH summer (Figure 4b), the winter circulation toward the winter pole (i.e., the south pole) in its upper part is

319 wide (extending to 60°N), deep (expanding up to z = ~100 km), and strong. In contrast, the
320 summer circulation toward the summer pole (i.e., the north pole) in its upper part is small and
321 within a limited latitudinal range of ~40°N–70°N with its top at z = ~60 km. Similar winter and
322 summer circulations are observed in the NH winter (Figure 4c). In the NH winter, a small and
323 weak clockwise circulation is also present at 50°S–80°S below z = ~30 km. The winter
324 circulation in the NH winter is stronger than that in the SH winter. It is worth noting that the
325 winter circulation in the NH winter extends to the south pole above z = ~50 km, whereas that in
326 the NH summer does not reach the north pole.

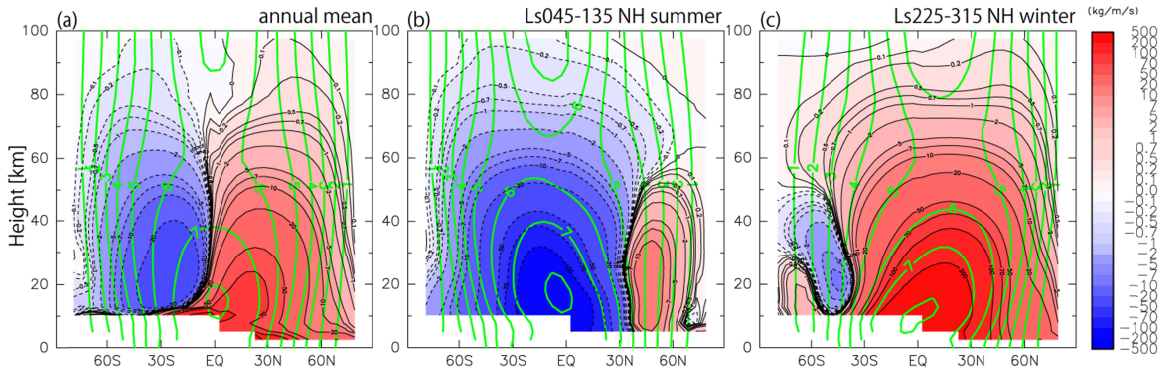

327

328 **Figure 4.** Latitude–height sections of zonal mean absolute angular momentum (green contours)
329 and zonal mean residual mean meridional stream function (colors): (**a**) the annual mean, (**b**) in
330 NH summer, and (**c**) in NH winter. Contour interval for absolute angular momentum is 0.5 ×
331 10^8 $m^2 s^{-1}$.

332 The structure of the annual mean climatology of $\bar{m}$, denoted by green contours in Figure
333 4, is nearly symmetric around the equator. In the mid- and high-latitude ranges of 30°S–90°S and
334 30°N–90°N, the $\bar{m}$ contours are almost vertical. In other words, $\bar{m}$ is nearly constant in the
335 vertical, whereas at low latitudes near 30°S/30°N, the contours are curved in the altitude range of
336 10–80 km. At latitudes lower than 30°S/30°N, the minimum $\bar{m}$ in the vertical is observed at z =
337 ~60 km and the $\bar{m}$ contours are not connected from the bottom to the displayed top of the
338 atmosphere. For the NH winter and NH summer, the $\bar{m}$ structure is broadly similar to that of the
339 annual mean climatology, reflecting the fast rotation of Mars. A notable difference from the
340 annual climatology is that the latitudinal range where the $\bar{m}$ contours originating from the low

latitudes of the NH and the SH are connected over the equator is shifted slightly toward the winter hemisphere.

The stream function of the residual mean circulation $\bar{\Psi}^*$ is almost parallel to the $\bar{m}$ contours at low latitudes at $z = 10$–80 km in the solstitial seasons. It is interesting to note that the strong $\bar{v}^*$ toward the winter pole over the equatorial region is in the region of the $\bar{m}$ minimum in the vertical in the low latitudes. Comparison of the distribution of $\bar{m}$ between MACDA and EMARS for Ls = ~270° in MY 24, presented in Waugh et al. (2016; their Figure 8) and focusing on a specific year and season, reveals that the distribution of $\bar{m}$ is not that similar for the two reanalysis datasets. The latitudinal range with the $\bar{m}$ minimum in the vertical is wider for EMARS than for MACDA. This difference is attributable to the differences in the distribution of the zonal mean zonal wind (their Figure 5). It is also noteworthy that an area where the $\bar{m}$ contours are horizontal is also observed in Earth's middle atmosphere but limited to a narrower latitudinal range than that in the Martian atmosphere (e.g., Haynes et al., 1991; Tomikawa et al., 2008).

4. Wave Forcing Associated with Resolved Waves (RWs) in EMARS

In this section, we identify the area where the residual mean flow crosses the isopleths of angular momentum, because wave forcing is necessary to drive the circulation in such an area. Then, the distribution of wave forcing associated with the RWs in the EMARS reanalysis data is examined in terms of EP flux divergence.

4.1 Residual mean mass stream functions and zonal mean absolute angular momentum

The MGCM results for the NH winter with realistic dust distribution, presented by Wilson (1997), are consistent with a nearly inviscid Hadley circulation expected from the conservation of absolute angular momentum (e.g., Held & Hou, 1980) below $z = 50$ km in the region of 60°S–60°N. In this region, the stream function and $\bar{m}$ surfaces are approximately parallel. It is evident from Figures 4a–c that the residual mean stream function and absolute angular momentum are approximately parallel in the limited latitudinal region of 40°S–30°N below $z = 50$ km in the NH summer and that of 30°S–50°N below $z = 45$ km in the NH winter. However, the residual mean circulation in the other latitudinal and height regions crosses the

absolute angular momentum contours, which means that the residual circulation should be driven by wave forcings there.

4.2 EP Flux Divergence

Figure 5 shows the climatology of total EP flux and its divergence (EPFD) in the meridional cross sections for the annual mean, NH summer, and NH winter. For the annual mean (Figure 5a), the distribution of EPFD is almost symmetric about the equator. Negative EPFD is observed around the mid- and high latitudes of both hemispheres for z = 20–80 km, whereas positive EPFD is evident in the low latitudes above z = 60 km and in high latitudes at z = 20–40 km. Generally, EPFD is positive below z = 20 km. For the NH summer (Figure 5b), large negative EPFD is observed at 20°S–80°S above z = 20 km, except at high latitudes below 40 km. Large negative EPFD is also present at ~ 60°N and z = ~40 km. The structure of EPFD for the NH winter (Figure 5c) is roughly symmetric around the equator, similar to that in the NH summer (Figure 5b). The difference between the two solstitial seasons is that the negative EPFD in the winter hemisphere in z = 40–80 km is stronger in the NH winter than in the NH summer.

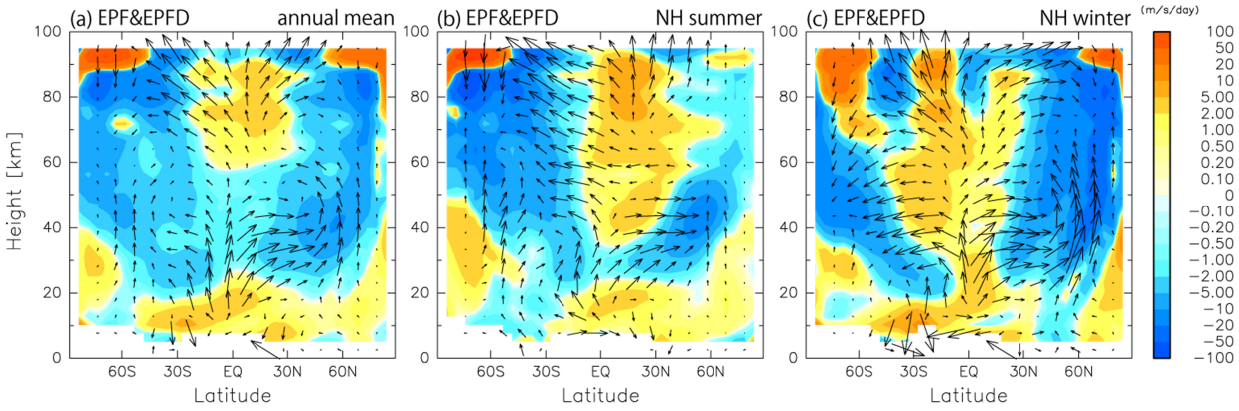

Figure 5. Latitude–height sections of EPFD of all components (colors) and EPF (vectors): (**a**) the annual mean, (**b**) in NH summer, and (**c**) in NH winter.

Figure 6 shows the climatology of the residual mean meridional flow overlaid with EPFD for the annual mean, NH summer, and NH winter. The relation between the wave forcing associated with RWs and the residual mean flow can be evaluated using the TEM equation described in section 2.2. Here, we assume that the zonal mean zonal wind tendency is zero for the annual mean or for the mean over the respective solstitial season. Then, the TEM equation is simplified as follows:

$$-\hat{f}\bar{v}^* \sim \frac{1}{\rho_0 a \cos\phi} \nabla \cdot \boldsymbol{F}_{(\mathrm{RW})}, \quad (17)$$

which shows that the Coriolis torque for the residual mean meridional flow is balanced by the wave forcing in the mid- and high latitudes. It should be noted that this simplified relation is not appropriate for analysis of equatorial regions where the Coriolis parameter is rather small. Figure 6 indicates that the residual mean meridional flow $\bar{v}^*$ is consistent with the EPFD in most mid- and high-latitude regions in terms of sign. This result is also consistent with the findings of a previous study suggesting that RW forcings drive the residual mean circulation (Hartogh et al., 2007). In both solstitial seasons, a winter hemispheric part of the strong flow toward the winter pole and a weak flow toward the summer pole in the SH correspond well to the negative EPFD (Figures 6b and 6c). A summer hemispheric part of the strong flow toward the winter pole also corresponds well to the positive EPFD in both solstitial seasons.

For quantitative analysis, it is necessary to consider not only the EPFD attributable to RWs in the reanalysis data, but also the wave forcing associated with UWs, including subgrid-scale GWs ($\nabla \cdot \boldsymbol{F}_{(\mathrm{UW})}$), as described in section 2.3. The contribution of UWs to the residual mean meridional circulation is examined in section 5.

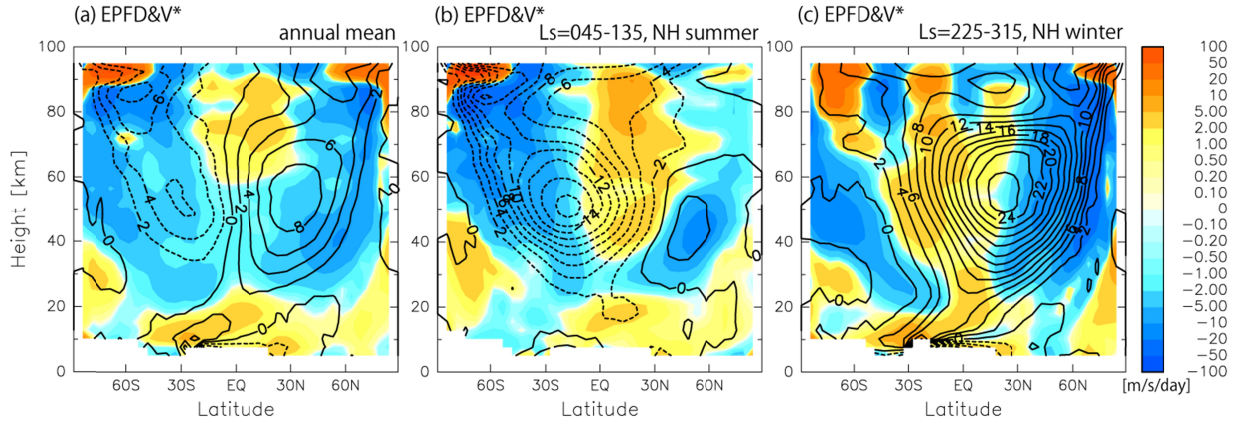

Figure 6. Latitude–height sections of EPFD of all RWs (colors) and residual mean meridional wind (contours): (**a**) the annual mean, (**b**) in NH summer, and (**c**) in NH winter. Contour interval for residual mean meridional wind is 2 m s^{-1}.

4.3 Role of the thermal tide and other waves

Figures 7a–c show climatology of the EPFD associated with tidal waves in the meridional cross sections for the annual mean, NH summer, and NH winter, and Figures 7d–f show that of the other waves. It is evident that the overall structure of the total EPFD is well explained by the contribution of tidal waves (Figures 7a–c) in all climatologies, except for the mid- and high-latitude regions, particularly in the winter hemisphere where the contribution of the other component is dominant (Figures 7e and 7f).

For the annual mean climatology, the total EPFD is mainly attributable to tidal waves above $z = 70$ km. In the altitude range of $z = 40$–70 km, the total EPFD is negative in most latitudes. At latitudes higher than 30°, this negative EPFD is attributable to the contribution of the other component, whereas the tidal wave contribution is large at lower latitudes. For $z = 20$–40 km, the negative area of total EPFD at low latitudes is mainly explained by the tidal component (Figure 7a), whereas the positive area at latitudes higher than 60° is mainly due to the other component (Figure 7d). Below $z = 20$ km, the tidal wave is the main contributor to the total EPFD.

For the NH summer, the EPFD attributable to the tidal component largely determines the total EPFD structure above $z = 70$ km at most latitudes (Figure 7b), whereas the contributions of both the tidal wave and the other component are large above $z = 70$ km at all latitudes in the NH winter (Figures 7c and 7f). The other component mainly contributes to the total EPFD in the mid- and high-latitude regions of the winter hemisphere in the entire altitude range, particularly in the NH winter. It is also worth noting that the EPFD attributable to the tidal component is largely negative at approximately $z = 40$–50 km in the summer hemisphere.

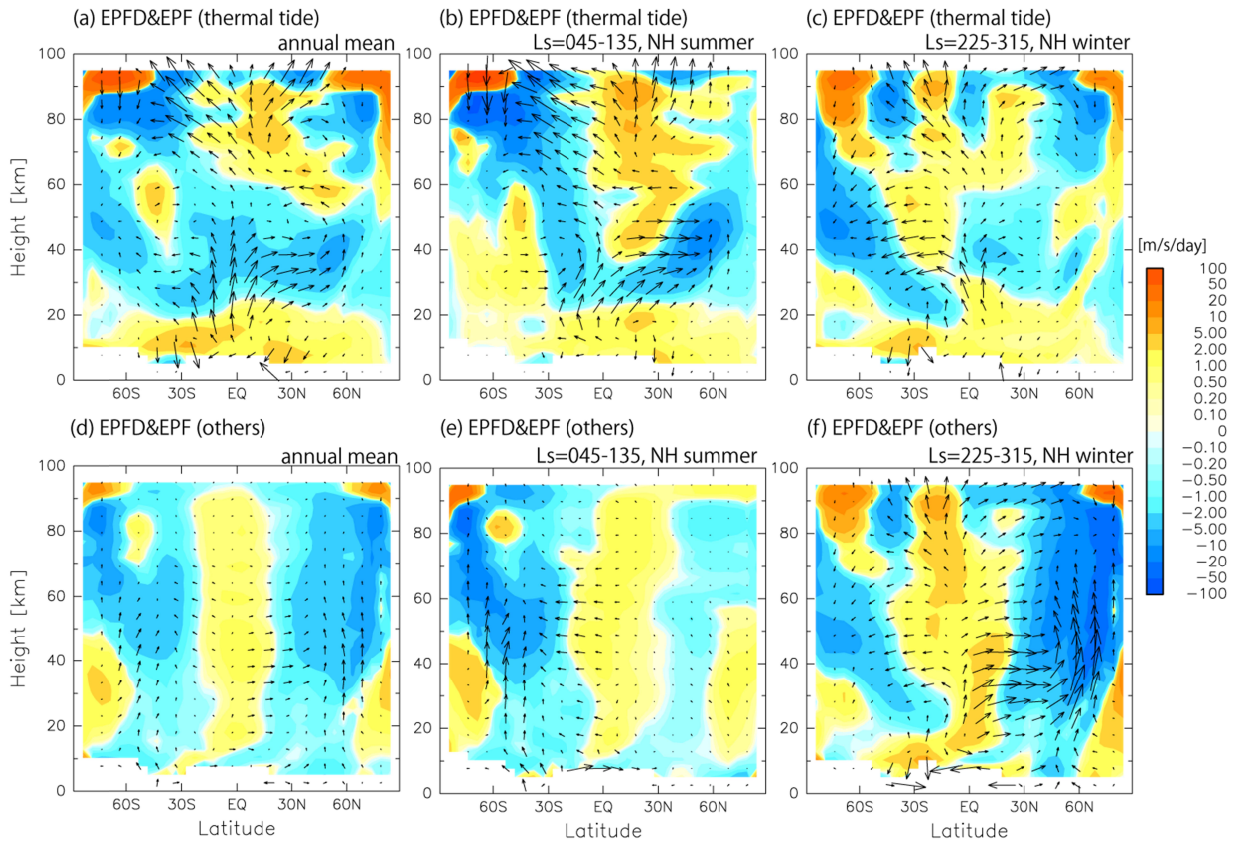

433

434 **Figure 7**. Latitude–height sections of EPFD associated with tidal component (colors) and EPF
435 (vectors): (**a**) the annual mean, (**b**) in NH summer, and (**c**) in NH winter. (**d**)–(**f**) Same as (**a**)–(**c**),
436 respectively, but for those associated with components other than the tidal component.

437 Figures 8a–8c show meridional cross sections of the latitudinal gradient of quasi-
438 geostrophic potential vorticity $\bar{q}_y$. Here, $\bar{q}_y$ is sometimes called the effective beta, which is
439 expressed as follows:

440 $$\bar{q}_y = \beta - \frac{1}{a^2}\frac{\partial}{\partial\phi}\left(\frac{1}{\cos\phi}\frac{\partial(\bar{u}\cos\phi)}{\partial\phi}\right) - \frac{1}{\rho_0}\frac{\partial}{\partial z}\left(\rho_0 \frac{f_0^2}{N^2}\frac{\partial\bar{u}}{\partial z}\right). \quad (18)$$

441 The presence of negative $\bar{q}_y$ is the necessary condition of barotropic and/or baroclinic instability
442 for fast rotating planets with $\beta > 0$ (e.g., Andrews et al., 1987). In the solstitial seasons, negative
443 $\bar{q}_y$ is observed at altitudes below $z = 50$ km at high latitudes in the winter hemisphere (Figures
444 8b and 8c), which is mainly attributable to the largely negative $-\frac{1}{a^2}\frac{\partial}{\partial\phi}\left(\frac{1}{\cos\phi}\frac{\partial(\bar{u}\cos\phi)}{\partial\phi}\right)$, i.e., the
445 second term on the right-hand side of Eq. (18), associated with the strong westerly jets (Figures

2e and 2f). In this area and above, upward EP flux is evident from the region of positive EPFD toward the region of negative EPFD (Figures 7e and 7f). This feature indicates that the waves associated with the upward EP flux are generated by baroclinic instability. In the NH winter, another region of weakly negative $\bar{q}_y$ is evident at latitudes lower than 40°N at $z = \sim$50 km. An area of quite weak and negative $\bar{q}_y$ is also present at approximately 30°S at $z = \sim$57 km in the NH summer. This area of negative $\bar{q}_y$, attributable to the third term on the right-hand side of Eq. (18), is related to the upper structure of the westerly jet in the winter hemisphere. Poleward EP fluxes in the winter hemisphere observed at latitudes approximately 30°N and above $z = \sim$30 km in the NH winter and above $z = \sim$40 km in the NH summer are likely due to waves generated by barotropic instability, as shown in many previous studies (e.g., Lewis et al., 2016).

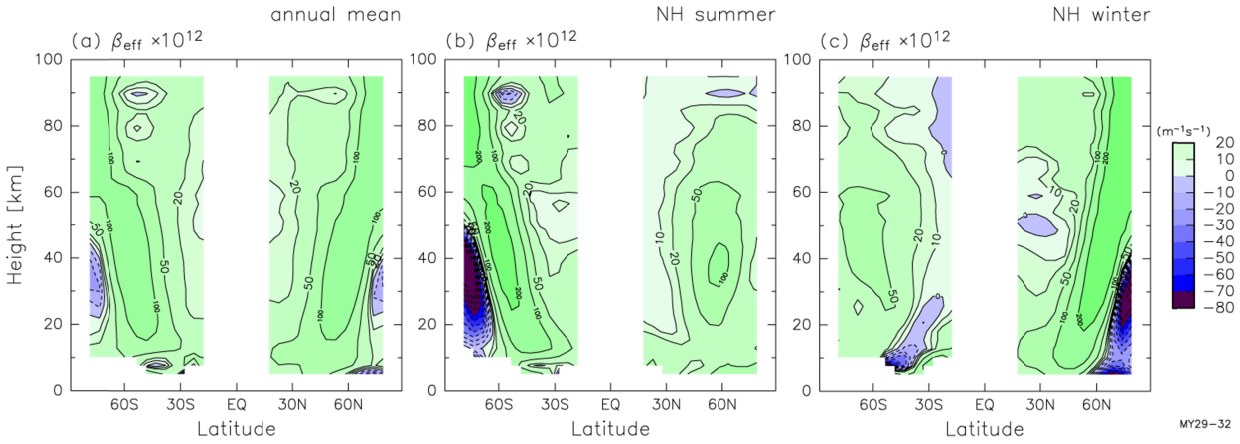

Figure 8. Latitude–height sections of $\bar{q}_y$: (**a**) the annual mean, (**b**) in NH summer, and (**c**) in NH winter. Contour interval is 10×10^{-12} m^{-1} s^{-1}.

5. Contribution of Unresolved Waves (UWs) to the Residual Circulation

Using the method described in the section 2.3, the stream function of the residual mean calculation $\overline{\Psi}^*$ is examined in terms of the directly estimated contribution by RWs ($\overline{\Psi}^*_{\nabla\cdot\mathbf{F}(\mathrm{RW})}(\phi, z)$) and the indirectly estimated contribution by UWs ($\overline{\Psi}^*_{\nabla\cdot\boldsymbol{F}(\mathrm{UW})}(\phi, z)$). As explained in section 2.3, the calculation is performed for the off-equatorial region where the $\bar{m}$ contours are connected all the way from the surface to the top of the altitude region displayed in Figure 4.

5.1 Annual mean climatology of the mass stream function

Figure 9 shows the annual mean climatology of $\overline{\Psi}^*(\phi, z)$, $\overline{\Psi}^*_{\nabla\cdot\mathbf{F}_{(\mathrm{RW})}}(\phi, z)$, and $\overline{\Psi}^*_{\nabla\cdot\mathbf{F}_{(\mathrm{UW})}}(\phi, z)$. The $\overline{\Psi}^*(\phi, z)$ structure of the annual mean climatology is almost symmetric about the equator (Figure 9a). It is interesting that most of the $\overline{\Psi}^*(\phi, z)$ structure is explained not by $\overline{\Psi}^*_{\nabla\cdot\mathbf{F}_{(\mathrm{RW})}}(\phi, z)$ but by $\overline{\Psi}^*_{\nabla\cdot\mathbf{F}_{(\mathrm{UW})}}(\phi, z)$. This is in marked contrast to the situation in Earth's stratosphere but similar to that in Earth's mesosphere (e.g., Plumb, 2002). However, it is worth nothing that even in the Earth stratosphere the summer hemispheric part of the deep branch of the Brewer–Dobson circulation is essentially driven by GWs (e.g., Okamoto et al., 2012). On Mars, the relative contributions of $\overline{\Psi}^*_{\nabla\cdot\mathbf{F}_{(\mathrm{RW})}}(\phi, z)$ and $\overline{\Psi}^*_{\nabla\cdot\mathbf{F}_{(\mathrm{UW})}}(\phi, z)$ to $\overline{\Psi}^*(\phi, z)$ also depend on latitude and altitude.

Although the contribution of UWs to $\overline{\Psi}^*(\phi, z)$ is dominant, that of RWs is also important in some areas in both hemispheres. The contribution of UWs tends to be larger at higher latitudes. Small reversed circulations observed in the high latitudes at altitudes of 20–50 km in $\overline{\Psi}^*(\phi, z)$ are due to RWs (i.e., $\overline{\Psi}^*_{\nabla\cdot\mathbf{F}_{(\mathrm{RW})}}(\phi, z)$) in their lower part (Figure 9b) and due to UWs (i.e., $\overline{\Psi}^*_{\nabla\cdot\mathbf{F}_{(\mathrm{UW})}}(\phi, z)$) in their upper part (Figure 9c). Above the altitude of z =50 km, the contribution of UWs mainly determines $\overline{\Psi}^*(\phi, z)$, whereas the contribution of RWs is small, particularly at high latitudes.

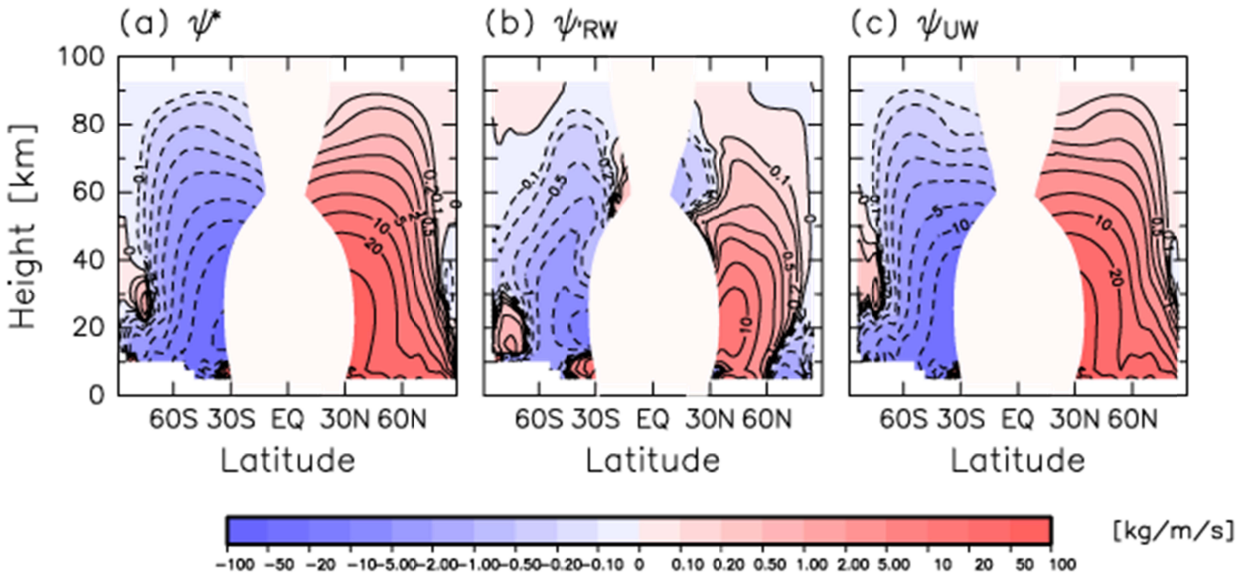

Figure 9 Latitude–height sections of the climatology of the annual mean stream function of (**a**) the residual mean flow, and the contribution of (**b**) RWs and (**c**) UWs.

5.2 Mass stream functions in the solstitial seasons

Figure 10 shows the climatology of $\overline{\Psi}^{*}(\phi, z)$, $\overline{\Psi}^{*}_{\nabla\cdot\mathbf{F}_{(\mathrm{RW})}}(\phi, z)$, and $\overline{\Psi}^{*}_{\nabla\cdot\mathbf{F}_{(\mathrm{UW})}}(\phi, z)$ for the NH summer. Similar to the annual mean climatology, the structure of $\overline{\Psi}^{*}(\phi, z)$ well resembles that of $\overline{\Psi}^{*}_{\nabla\cdot\mathbf{F}_{(\mathrm{UW})}}(\phi, z)$. In the summer hemisphere (i.e., the NH), a clockwise circulation observed

491 at altitudes below $z = 50$ km in $\overline{\Psi}^*(\phi, z)$ reflects almost equal contributions by the RW and the
492 UW components, although the RW contribution is slightly larger. The summer hemispheric part
493 of the counterclockwise circulation toward the winter pole at its upper part is largely extended to
494 high latitudes at $z > 50$ km and has the largest contribution from the UW component. In the
495 winter hemisphere (i.e., the SH), the UW contribution to the counterclockwise circulation is
496 several times larger than the RW contribution in the region of 40°–80°S. It is interesting to note
497 that a small clockwise circulation is present at approximately 60°–80°S below the altitude of 40
498 km in $\overline{\Psi}^*_{\nabla\cdot\mathbf{F}_{(\mathrm{RW})}}(\phi, z)$. This circulation is largely canceled by $\overline{\Psi}^*_{\nabla\cdot\mathbf{F}_{(\mathrm{UW})}}(\phi, z)$ and is therefore not
499 observed in $\overline{\Psi}^*(\phi, z)$. It should be noted that $\Psi_{\overline{u}_t}(\phi, z)$ is minor in most regions in this season
500 compared with $\overline{\Psi}^*_{\nabla\cdot\mathbf{F}_{(\mathrm{RW})}}(\phi, z)$ and $\overline{\Psi}^*_{\nabla\cdot\mathbf{F}_{(\mathrm{UW})}}(\phi, z)$; hence, it is not shown here.

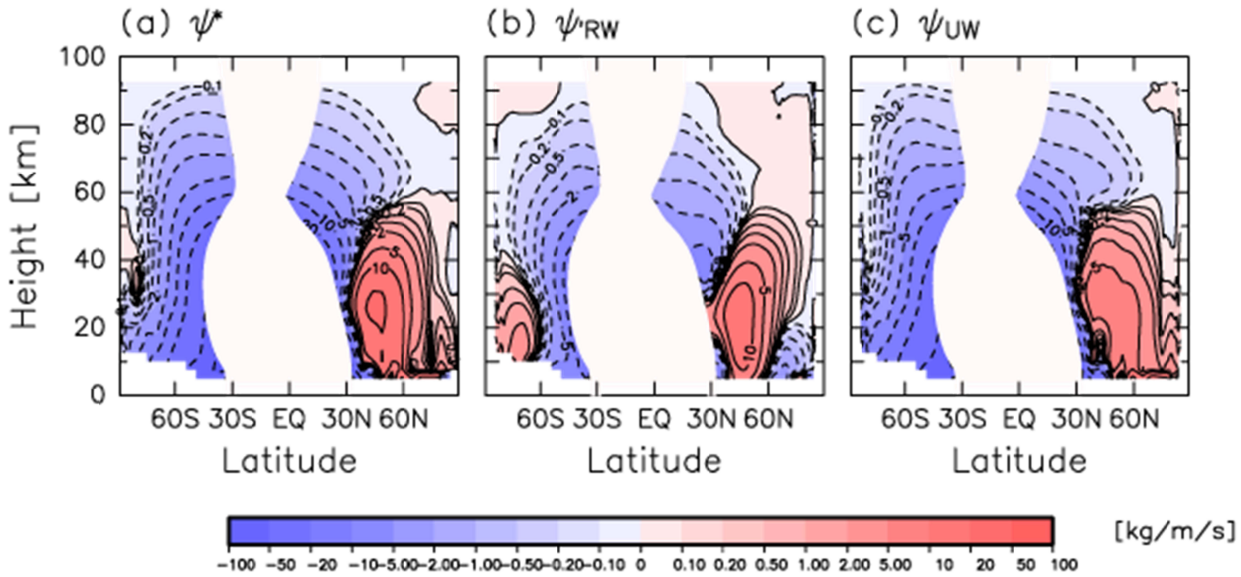

Figure 10 Same as Figure 9 but for the NH summer.

Figure 11 shows the climatology of $\overline{\Psi}^*(\phi, z)$, $\overline{\Psi}^*_{\nabla\cdot\mathbf{F}_{(\mathrm{RW})}}(\phi, z)$, and $\overline{\Psi}^*_{\nabla\cdot\mathbf{F}_{(\mathrm{UW})}}(\phi, z)$ for the NH winter. Similar to the annual mean and NH summer climatologies, the structure of $\overline{\Psi}^*(\phi, z)$ well resembles that of $\overline{\Psi}^*_{\nabla\cdot\mathbf{F}_{(\mathrm{UW})}}(\phi, z)$. A notable difference from the structure in the NH summer is that the counterclockwise circulation observed in $\overline{\Psi}^*(\phi, z)$ over the mid- and high latitudes of the summer hemisphere (i.e., the SH) is explained by the RW contribution. The structure of $\overline{\Psi}^*_{\nabla\cdot\mathbf{F}_{(\mathrm{UW})}}(\phi, z)$ is dominated by a single, equator-crossing large clockwise cell toward the winter

pole at its upper part extending to altitudes higher than $z = 90$ km. In contrast, $\overline{\Psi}^*_{\nabla\cdot\mathbf{F}_{(\mathrm{RW})}}(\phi, z)$ consists of two large cells: a large clockwise winter circulation crossing the equator and a counterclockwise summer circulation restricted to mid- and high latitudes at approximately 60°S. For the winter circulation, the contribution of UWs is several times larger than that of RWs; hence, the structure of $\overline{\Psi}^*(\phi, z)$ is predominantly determined by $\overline{\Psi}^*_{\nabla\cdot\mathbf{F}_{(\mathrm{UW})}}(\phi, z)$. A small clockwise circulation presented in $\overline{\Psi}^*(\phi, z)$ at 60°S–80°S at altitudes below 30 km (Figure 11a) is attributable to $\overline{\Psi}^*_{\nabla\cdot\mathbf{F}_{(\mathrm{UW})}}(\phi, z)$ (Figure 11c). It should be noted that the strength of $\Psi_{\overline{u}_t}(\phi, z)$ is weak, similar to that in the NH summer and thus it is also not shown here.

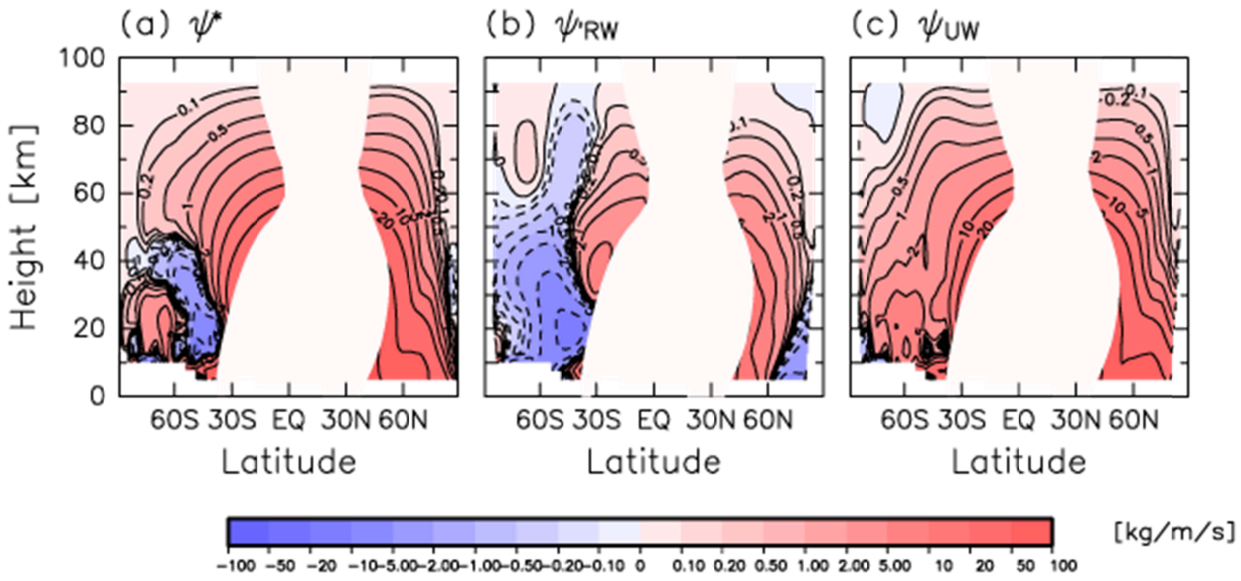

517

518 **Figure 11** Same as Figure 9 but for the NH winter.

519 **6. Summary and Concluding Remarks**

520 The climatology of the residual mean circulation of Mars over the four Mars years of MY
521 29–32 was examined using the recently available EMARS reanalysis dataset. During this four
522 MY period, no global dust storm occurred. Using the TEM equation system, the analysis focused
523 on the annual mean and the two solstitial seasons of the NH summer and winter. The relative

roles of RW and UW forcings in the residual mean circulation in mid- and high-latitude regions were evaluated quantitatively.

In the altitude range of 10–90 km, the structures of $\bar{v}$ and $\bar{v}^*$ were quantitatively similar in the annual mean, NH summer, and NH winter climatologies. This finding indicates that the Stokes correction is generally small and hence, the wave forcing caused by upward propagating Rossby waves is also small, which is strikingly different to the situation in Earth's stratosphere. For the solstitial seasons, a residual mean meridional flow from the summer hemisphere to the winter hemisphere at approximately z =50 km is evident, similar to the deep branch of the Brewer–Dobson circulation in Earth's stratosphere. The latitudinal expansion of the winter circulation to the summer hemisphere is wider on Mars. In the NH winter, the residual mean northward flow amounts to 28.5 m s^{-1} at its peak at 20°N (z = ~55 km), whereas the southward flow in the NH summer is slightly weaker and amounts to 19.2 m s^{-1} at its peak at 20°S (z = ~50 km). The magnitude of these meridional flows is notably stronger than of those in Earth's middle atmosphere. Interestingly, the $\bar{m}$ minimum in the vertical is observed over the equator at z = 50–70 km. The strong $\bar{v}^*$ toward the winter pole in the solstitial seasons crosses the equator in this $\bar{m}$ minimum region. At mid- and high-latitude regions, the residual mean flow crosses the isopleths of angular momentum, indicating that wave forcing is necessary to drive the meridional circulation there. The distribution of wave forcing associated with RWs was examined in terms of EPFD. The entire EPFD structure is mainly attributable to the contribution of the thermal tides for the annual mean, NH summer, and NH winter climatologies. However, the wave forcing in mid- and high latitudes in winter is dominated by the contribution of RWs other than the tidal component. The distribution of $\bar{v}^*$ is consistent with the sign of the EPFD associated with RWs in mid- and high latitudes. The $\bar{q}_y$ distribution suggests that these RWs other than the tidal component are generated by baroclinic or barotropic instability depending on the dominant region.

Furthermore, the role of the UW component in the meridional circulation was evaluated quantitatively. The contribution of RWs was calculated directly from the EPFD, whereas that of the UWs, including subgrid-scale GWs, was estimated indirectly using the zonal momentum equation of the TEM equation system following the method by Sato and Hirano (2019). This indirect estimation is possible only for mid- and high-latitude regions where the $\bar{m}$ contours are

connected from the ground to the top altitude. Results suggest that the contribution of UWs is comparable to or larger than that of RWs for mid- and high latitudes. The fact that small-scale disturbances are the main driver is in marked contrast to the Earth's stratosphere but similar to the Earth's mesosphere. The entire structure of the residual mean circulation is mainly determined by the contribution of UWs, especially at altitudes above $z = 60$ km, whereas the contribution of RWs is also important at $z < \sim 60$ km for the annual mean, NH summer, and NH winter climatologies. In the NH winter, the residual mean counterclockwise summer circulation in the SH is explained by the RW contribution, although its large part is canceled by the UW contribution. These results illustrate the importance of UWs in the climatological features of the residual mean circulation in mid- and high-latitude regions.

In future work, we will investigate the climatology of the equinox seasons, i.e., NH spring and NH autumn, when the zonal wind tendency attributable to the seasonal time variation of solar radiative heating is important (Sato & Hirano, 2019). The robustness of the findings also needs to be confirmed using another reanalysis dataset. The present study examined the climatology of relatively calm years. However, it is expected that years with a global dust storm, such as MY 25, which represents one of the most spectacular events in the Martian atmosphere, will exhibit different and/or enhanced characteristics from the climatology described in this study. The residual mean circulation for MY 25 is one such important case that merits further detailed examination.

Acknowledgments

All figures in this study were drawn using Dennou Club Library. This work was supported by JSPS KAKENHI Grant Number JP22H00169.

Open Research

Version 1.0 of the Ensemble Mars Atmosphere Reanalysis System (EMARS) used in our study is preserved at https://doi.org/10.18113/D3W375 and developed openly at Penn State Data Commons.

References

Andrews, D. G., Holton, J. R., and Leovy, C. B. (1987) *Middle Atmosphere Dynamics*, Academic Press, 489 pp. San Diego, Calif.

583 Angelats i Coll, M., Forget, F., López-Valverde, M. A., & González-Galindo, F. (2005). The first
584 Mars thermospheric general circulation model: The Martian atmosphere from the ground
585 to 240 km. Geophysical Research Letters, 32(4). https://doi.org/10.1029/2004GL021368

586 Barnes, J. R. (1990). Possible effects of breaking gravity waves on the circulation of the middle
587 atmosphere of Mars. Journal of Geophysical Research: Solid Earth, 95(B2), 1401–1421.
588 https://doi.org/10.1029/JB095iB02p01401

589 Barnes, J. R., & Haberle, R. M. (1996). The Martian Zonal-Mean Circulation: Angular
590 Momentum and Potential Vorticity Structure in GCM Simulations. *Journal of the*
591 *Atmospheric Sciences*, *53*(21), 3143–3156. https://doi.org/10.1175/1520-
592 0469(1996)053<3143:TMZMCA>2.0.CO;2

593 Barnes, J. R., Haberle, R. M., Wilson, R. J., Lewis, S. R., Murphy, J. R., & Read, P. L. (2017).
594 The Global Circulation. In F. Forget, M. D. Smith, R. T. Clancy, R. W. Zurek, & R. M.
595 Haberle (Eds.), *The Atmosphere and Climate of Mars* (pp. 229–294). Cambridge,
596 Cambridge University Press. https://doi.org/10.1017/9781139060172.009

597 Collins, M., Lewis, S. R., & Read, P. L. (1997). Gravity wave drag in a global circulation model
598 of the Martian atmosphere: Parameterisation and validation. Advances in Space
599 Research, 19(8), 1245–1254. https://doi.org/10.1016/S0273-1177(97)00277-9

600 Dunkerton, T. J. (1983). The Conservation of Pseudoenergy in Lagrangian Time-Mean Flow.
601 Journal of the Atmospheric Sciences, 40(11), 2623–2629. https://doi.org/10.1175/1520-
602 0469(1983)040<2623:TCOPIL>2.0.CO;2

603 Forget, F., Hourdin, F., Fournier, R., Hourdin, C., Talagrand, O., Collins, M., Lewis, S. R., Read,
604 P. L., & Huot, J.-P. (1999). Improved general circulation models of the Martian
605 atmosphere from the surface to above 80 km. *Journal of Geophysical Research: Planets*,
606 *104*(E10), 24155–24175. https://doi.org/10.1029/1999JE001025

607 Fritts, D. C., Wang, L., & Tolson, R. H. (2006). Mean and gravity wave structures and variability
608 in the Mars upper atmosphere inferred from Mars Global Surveyor and Mars Odyssey
609 aerobraking densities. Journal of Geophysical Research: Space Physics, 111(A12).
610 https://doi.org/10.1029/2006JA011897

611 Greybush, S. J., Wilson, R. J., Hoffman, R. N., Hoffman, M. J., Miyoshi, T., Ide, K.,
612 McConnochie, T., & Kalnay, E. (2012). Ensemble Kalman filter data assimilation of
613 Thermal Emission Spectrometer temperature retrievals into a Mars GCM. *Journal of*
614 *Geophysical Research: Planets*, *117*(E11). https://doi.org/10.1029/2012JE004097

615 Greybush, S. J., Kalnay, E., Wilson, R. J., Hoffman, R. N., Nehrkorn, T., Leidner, M.,
616 Eluszkiewicz, J., Gillespie, H. E., Wespetal, M., Zhao, Y., Hoffman, M., Dudas, P.,
617 McConnochie, T., Kleinböhl, A., Kass, D., McCleese, D., & Miyoshi, T. (2019). The
618 Ensemble Mars Atmosphere Reanalysis System (EMARS) Version 1.0. *Geoscience Data*
619 *Journal*, *6*(2), 137–150. https://doi.org/10.1002/gdj3.77

620 Greybush, S. J., Kalnay, E., Wilson, R. J., Hoffman, R. N., Nehrkorn, T., Leidner, M.,
621 Eluszkiewicz, J., Gillespie, H. E., Wespetal, M., Zhao, Y., Hoffman, M., Dudas, P.,
622 McConnochie, T., Kleinböhl, A., Kass, D., McCleese, D., & Miyoshi, T. (2019). The
623 Ensemble Mars Atmosphere Reanalysis System (EMARS) (Version 1) [Dataset].
624 https://doi.org/10.18113/D3W375

Haberle, R., Clancy, R., Forget, F., Smith, M., & Zurek, R. (2017). Introduction. In R. Haberle, R. Clancy, F. Forget, M. Smith, & R. Zurek (Eds.), The Atmosphere and Climate of Mars (Cambridge Planetary Science, pp. 1-2). Cambridge: Cambridge University Press. doi:10.1017/9781139060172.001

Hartogh, P., Medvedev, A. S., & Jarchow, C. (2007). Middle atmosphere polar warmings on Mars: Simulations and study on the validation with sub-millimeter observations. *Planetary and Space Science*, *55*(9), 1103–1112. https://doi.org/10.1016/j.pss.2006.11.018

Haynes, P. H., McIntyre, M. E., Shepherd, T. G., Marks, C. J., & Shine, K. P. (1991). On the "Downward Control" of Extratropical Diabatic Circulations by Eddy-Induced Mean Zonal Forces. *Journal of the Atmospheric Sciences*, *48*(4), 651–678. https://doi.org/10.1175/1520-0469(1991)048<0651:OTCOED>2.0.CO;2

Held, I. M., & Hou, A. Y. (1980). Nonlinear Axially Symmetric Circulations in a Nearly Inviscid Atmosphere. Journal of the Atmospheric Sciences, 37(3), 515–533. https://doi.org/10.1175/1520-0469(1980)037<0515:NASCIA>2.0.CO;2

Hoffman, M. J., Greybush, S. J., John Wilson, R., Gyarmati, G., Hoffman, R. N., Kalnay, E., Ide, K., Kostelich, E. J., Miyoshi, T., & Szunyogh, I. (2010). An ensemble Kalman filter data assimilation system for the martian atmosphere: Implementation and simulation experiments. *Icarus*, *209*(2), 470–481. https://doi.org/10.1016/j.icarus.2010.03.034

Holton, J. R., Haynes, P. H., McIntyre, M. E., Douglass, A. R., Rood, R. B., & Pfister, L. (1995). Stratosphere-troposphere exchange. *Reviews of Geophysics*, *33*(4), 403–439. https://doi.org/10.1029/95RG02097

Joshi, M. M., Lawrence, B. N., & Lewis, S. R. (1995). Gravity wave drag in three-dimensional atmospheric models of Mars. Journal of Geophysical Research: Planets, 100(E10), 21235–21245. https://doi.org/10.1029/95JE02486

Kuroda, T., Medvedev, A. S., Hartogh, P., & Takahashi, M. (2009). On Forcing the Winter Polar Warmings in the Martian Middle Atmosphere during Dust Storms. *Journal of the Meteorological Society of Japan. Ser. II*, *87*(5), 913–921. https://doi.org/10.2151/jmsj.87.913

Lewis, S. R., Collins, M., Read, P. L., Forget, F., Hourdin, F., Fournier, R., Hourdin, C., Talagrand, O., & Huot, J.-P. (1999). A climate database for Mars. *Journal of Geophysical Research: Planets*, *104*(E10), 24177–24194. https://doi.org/10.1029/1999JE001024

Lewis, S. R., & Read, P. L. (2003). Equatorial jets in the dusty Martian atmosphere. *Journal of Geophysical Research: Planets*, *108*, 5034. https://doi.org/10.1029/2002JE001933

Lewis, S. R., Mulholland, D. P., Read, P. L., Montabone, L., Wilson, R. J., & Smith, M. D. (2016). The solsticial pause on Mars: 1. A planetary wave reanalysis. Icarus, 264, 456–464. https://doi.org/10.1016/j.icarus.2015.08.039

Magalhães, J. A., Schofield, J. T., & Seiff, A. (1999). Results of the Mars Pathfinder atmospheric structure investigation. Journal of Geophysical Research: Planets, 104(E4), 8943–8955. https://doi.org/10.1029/1998JE900041

McCleese, D. J., Schofield, J. T., Taylor, F. W., Calcutt, S. B., Foote, M. C., Kass, D. M., Leovy, C. B., Paige, D. A., Read, P. L., & Zurek, R. W. (2007). Mars Climate Sounder: An investigation of thermal and water vapor structure, dust and condensate distributions in the atmosphere, and energy balance of the polar regions. *Journal of Geophysical Research: Planets*, *112,* E05S04. https://doi.org/10.1029/2006JE002790

Mitchell, D. M., Montabone, L., Thomson, S., & Read, P. L. (2015). Polar vortices on Earth and Mars: A comparative study of the climatology and variability from reanalyses. *Quarterly Journal of the Royal Meteorological Society*, *141*(687), 550–562. https://doi.org/10.1002/qj.2376

Montabone, L., Marsh, K., Lewis, S. R., Read, P. L., Smith, M. D., Holmes, J., Spiga, A., Lowe, D., & Pamment, A. (2014). The Mars Analysis Correction Data Assimilation (MACDA) Dataset V1.0. Geoscience Data Journal, 1(2), 129–139. https://doi.org/10.1002/gdj3.13

Okamoto, H., & Shōji, M. (2012). Trajectories of fluid particles in a periodic water wave. Philosophical Transactions of the Royal Society A: Mathematical, Physical and Engineering Sciences, 370(1964), 1661–1676. https://doi.org/10.1098/rsta.2011.0447

Plumb, R. A. (2002). Stratospheric Transport. Journal of the Meteorological Society of Japan. Ser. II, 80(4B), 793–809. https://doi.org/10.2151/jmsj.80.793

Randel, W. J., Garcia, R. R., & Wu, F. (2002). Time-Dependent Upwelling in the Tropical Lower Stratosphere Estimated from the Zonal-Mean Momentum Budget. Journal of the Atmospheric Sciences, 59(13), 2141–2152. https://doi.org/10.1175/1520-0469(2002)059<2141:TDUITT>2.0.CO;2

Read, P. L. (2011). Dynamics and circulation regimes of terrestrial planets. Planetary and Space Science, 59(10), 900–914. https://doi.org/10.1016/j.pss.2010.04.024

Read, P. L., Lewis, S. R., & Mulholland, D. P. (2015). The physics of Martian weather and climate: A review. *Reports on Progress in Physics*, *78*(12), 125901. https://doi.org/10.1088/0034-4885/78/12/125901

Sato, K., Kinoshita, T., & Okamoto, K. (2013). A New Method to Estimate Three-Dimensional Residual-Mean Circulation in the Middle Atmosphere and Its Application to Gravity Wave–Resolving General Circulation Model Data. *Journal of the Atmospheric Sciences, 70(12)*, 3756–3779. https://doi.org/10.1175/JAS-D-12-0352.1

Sato, K., & Hirano, S. (2019). The climatology of the Brewer–Dobson circulation and the contribution of gravity waves. *Atmospheric Chemistry and Physics*, *19*(7), 4517–4539. https://doi.org/10.5194/acp-19-4517-2019

Smith, M. D. (2004). Interannual variability in TES atmospheric observations of Mars during 1999–2003. Icarus, 167(1), 148–165. https://doi.org/10.1016/j.icarus.2003.09.010

Tomikawa, Y., Sato, K., Watanabe, S., Kawatani, Y., Miyazaki, K., & Takahashi, M. (2008). Wintertime temperature maximum at the subtropical stratopause in a T213L256 GCM. Journal of Geophysical Research: Atmospheres, 113(D17). https://doi.org/10.1029/2008JD009786

Waugh, D. W., Toigo, A. D., Guzewich, S. D., Greybush, S. J., Wilson, R. J., & Montabone, L. (2016). Martian polar vortices: Comparison of reanalyses. *Journal of Geophysical Research: Planets*, *121*(9), 1770–1785. https://doi.org/10.1002/2016JE005093

Wilson, R. J., & Hamilton, K. (1996). Comprehensive Model Simulation of Thermal Tides in the Martian Atmosphere. *Journal of the Atmospheric Sciences*, *53*(9), 1290–1326. https://doi.org/10.1175/1520-0469(1996)053<1290:CMSOTT>2.0.CO;2

Wilson, R. J. (1997). A general circulation model simulation of the Martian polar warming. *Geophysical Research Letters*, *24*(2), 123–126. https://doi.org/10.1029/96GL03814

Yasui, R., Sato, K., & Tsutsumi, M. (2016). Seasonal and Interannual Variation of Mesospheric Gravity Waves Based on MF Radar Observations over 15 Years at Syowa Station in the Antarctic. *Sola*, *12*, 46–50. https://doi.org/10.2151/sola.2016-010